

# Synthesis structural and anti-microbial characterization of nanostructured doped tin oxide

A.M. Roychaudhury<sup>1</sup>, Utsa Debnath<sup>1</sup>, Sujay Munshi<sup>2</sup>, Goutam Kumar Basak<sup>3</sup>, Abhigyan Dutta<sup>4</sup>, S. Masanta<sup>5</sup>, Achintya Singha<sup>5</sup>, Aritra Banerjee<sup>6</sup>, Debtanu Ghosh<sup>7</sup>, Partha Chatterjee<sup>7</sup>, and Apurba Kanti Deb<sup>2\*</sup>

## Abstract

Nanocrystalline boron doped tin oxide and boron and silver co-doped SnO<sub>2</sub> was successfully prepared by using simple sol-gel method. The structural property of as-prepared nanocrystalline materials was investigated by using X-ray powder diffraction, Raman spectroscopy, Fourier transform infrared spectroscopy and scanning electron microscopy. The infrared spectra of the prepared samples showed an incorporation of B and Ag in the SnO<sub>2</sub> nanocrystals. The X-ray powder diffraction pattern of the as prepared sample demonstrated the formation of a rutile structure of SnO<sub>2</sub> nanocrystallites with particle size of 35 nm and 98 nm for boron doped and co-doped samples respectively. The two different Sn-O bond distances are found to be varying in a different manner for the doped samples unlike pristine samples. A significant lattice microstrain was observed for co-doped samples indicating local lattice distortion. The prepared samples showed significant anti-microbial activities against some Gram-Positive & Gram-Negative bacteria in both water and DMSO medium. The prepared materials can be effective for water remediation.

## Keywords

Nanocrystalline doped SnO<sub>2</sub>, X-ray powder diffraction, Rietveld analysis, Raman and Fourier transform infrared Spectroscopy, Anti-microbial activity.

<sup>1</sup> Department of Chemistry, Raiganj University, Raiganj, Uttar Dinajpur 733134, India

<sup>2</sup> Department of Physics, Raiganj University, Raiganj, Uttar Dinajpur 733134, India

<sup>3</sup> Department of Microbiology, Raiganj University, Raiganj, Uttar Dinajpur 733134, India

<sup>4</sup> Department of Physics, University of Burdwan, Burdwan, 713 104, India

<sup>5</sup> Department of Physics, Bose Institute, 93/1, APC Road, Kolkata 700009, India

<sup>6</sup> Department of Physics, University of Calcutta, 92 A P C Road, Kolkata-700 009, India

<sup>7</sup> Department of Physics, Vivekananda Mahavidyalaya, Haripal, Hooghly 712405, India

\*Corresponding author: deb.apurba@gmail.com

## 1. Introduction

In the past decade due to rapid industrialisation and resultant indiscriminate pollution of water bodies grave concern has developed among the scientists and people in general. Outbreaks of infectious diseases caused by pathogenic bacteria and the concomitant increase in antibiotic resistance of bacteria [1], much attention in pharmaceutical and fields has been focused on creating new antibacterial agents [2].

In recent years, nano-dimensional inorganic antibacterial materials is projected as potential candidates for application in pharmaceutical field owing to their high surface-to-volume ratio and their novel physico-chemical properties on the nano-scale level [3,4]. Several nano-sized antibacterial materials are reported in the literature [5–7]. Most prominent among them are nano-Ag, nano-TiO<sub>2</sub>, nano-ZnO etc. It may be argued that although nanocrystalline silver has powerful antimicrobial activity, it is toxic to human cell.

The rutile tin dioxide phase has unique electrical properties

such as wide band gap ( $E_g=3.64\text{eV}$ , at 330K) and n-type semi conductivity arising out of oxygen vacancies. The band gap in tin dioxide may be altered by doping (cation, anion and co-doping) to meet the desired expectations. In the era of nanotechnology, tin oxide finds its important applications in the field of semiconductor, catalysis, optoelectronic device, anti-static coating, antimicrobial and gas sensor activities [8–13]. Nano-sized tin oxide materials have been reported to possess some specific properties and advantages of high sensitivity, including conductivity, high degree of transparency in the visible region, in addition to mechanical and chemical stabilities [14].

Recently there has been a growing interest in pure and doped SnO<sub>2</sub> for its uses in anti-microbial properties and water remediation. The anti-bacterial properties of SnO<sub>2</sub> have been observed in nano – SnO<sub>2</sub> particles synthesized by using DNA as capping agent [15]. The antibacterial properties were studied against three bacterial strains namely, Staphylococcus aureus (ATCC 9144), Shigella flexneri (ATCC 2908) and Escherichia

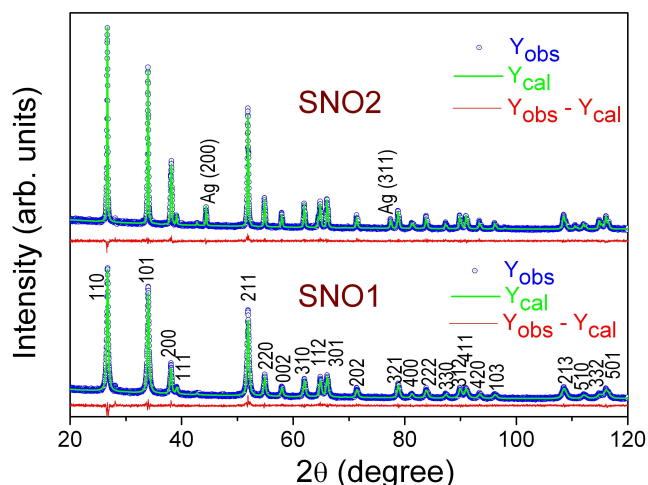


**Figure 1.** Rietveld fitted X-ray powder diffraction pattern of SNO1 and SNO2 samples along with the residuals.

Coli. Nanoscale SnO<sub>2</sub>, SnS<sub>2</sub> and SnO<sub>2</sub>/SnS<sub>2</sub> synthesized by hydrothermal method [16] showed photocatalytic, antibacterial and antifungal characteristics. The SnO<sub>2</sub>/SnS<sub>2</sub> composite showed enhanced photocatalytic, antibacterial and antifungal activity compared with pure SnO<sub>2</sub> and SnS<sub>2</sub>. Another group observed good antimicrobial activity in pure SnO<sub>2</sub> prepared by microwave-assisted solution method [17].

Several metallic and non-metallic dopant atoms, such as Ag [18–20], B [21, 22], Co [23], etc. has been considered in the literature. However, studies on B-doped SnO<sub>2</sub> is rare. One group of researchers [21] synthesized boron-doped SnO<sub>2</sub> (BTO) thin films by spray pyrolysis technique. The orientation of the BTO films changes from plane (110) to (101) with the increasing boron concentration. It was also observed that the boron ions occupy the interstitial site in SnO<sub>2</sub> lattice, which play the role of donor of free electrons. With increasing boron concentration boron ions start to replace the tin ions of lattice. Another potent application of Boron-doped tin dioxide (B-doped SnO<sub>2</sub>) films is to enhance the photodegradation of certain organic pollutants [22], under visible light irradiation. Co doped SnO<sub>2</sub> nanoparticles of average size 30–40 nm were reported to be synthesized chemically by some authors [23]. The photocatalytic and antimicrobial activities increased doping concentration.

Various methods used to synthesize SnO<sub>2</sub> nanostructures include Hydrothermal methods [24], Polymeric [25], Organometallic precursor synthesis [26], Sonication [27, 28], Microwave [29, 30], Surfactant-mediated method [31] etc. The sol-gel method is a simple technique to synthesize high purity, homogeneous, stoichiometrically controlled doped and co-doped nanocrystalline materials at a low cost. In sol-gel process, the precursor solution is transformed into an inorganic solid by dispersion of colloidal particles in a sol and then conversion of sol into gel [32].

In the present communication we would like to focus on both a non-metal B and a metal Ag as a dopant element in SnO<sub>2</sub> ma-

trices and study their effects on structural, microstructural and bactericidal properties. It is reported that Ag-SnO<sub>2</sub> nanocomposites show good antibacterial property [20]. B-doped SnO<sub>2</sub> shows good photocatalytic activity under both UV and visible light irradiation [22]. However, to the best of knowledge of the author antimicrobial property of B doped SnO<sub>2</sub> has not been reported in the literature. The silver doped tin dioxide shows effective Anti-microbial activities against some Gram-Positive and Gram-Negative Bacteria. It was reported by the combined studies of electron microscopy and X-Ray microanalysis that after Ag<sup>+</sup> treatment, the cytoplasm membrane was detached from the bacterial cell wall. A remarkable electron-light region appeared in the center of the cells, which contained DNA molecules. The existence of elements of silver and sulphur, in the electron dense granules and in cytoplasm, detected by X-Ray microanalysis suggested the antimicrobial mechanism of silver. DNA loses its replication ability and the protein become inactivated after Ag<sup>+</sup> treatment. In the present work, we have prepared boron doped and boron and silver co-doped SnO<sub>2</sub> by simple Sol-Gel method. Different characterization techniques such as x-ray powder diffraction (XRPD), Raman Spectroscopy, Fourier transform infrared spectroscopy (FTIR), scanning electron microscopy has been used for structural and microstructural parameters. The antibacterial activity of doped SnO<sub>2</sub> has been assessed against some important Gram-Positive and Gram-Negative Bacterial strains.

## 2. Experimental procedure

### 2.1 Sample preparation

For the preparation of boron doped SnO<sub>2</sub> (hereafter referred to as SNO1 sample), 1.1281 g of SnCl<sub>2</sub> (SnCl<sub>2</sub>·2H<sub>2</sub>O, AR, Merck) was dissolved in 50 mL of distilled water to get the clear solution. Then dilute NH<sub>4</sub>OH (1:1) was added to it drop by drop and a white precipitate was observed. The precipitate was filtered through G4 Gooch Crucible and the filtrate was washed with hot water. The precipitate was dissolved in dilute Acetic Acid (LR, Nice Chemicals) and 0.3091 g of Boric Acid (LR, Nice Chemicals) was added to it. The mixture was then added to the solution PVA solution, prepared by dissolving 2 g of PVA (n= approx. 2000, SD fine) into 50 mL distilled water. This solution was then stirred on a magnetic stirrer for 3 hours at 80° C. After that, it was kept in a hot-air oven at 90° C and then it was kept in the furnace at 800° C for 2 hours.

To prepare the boron and silver co-doped samples (hereafter referred to as SNO<sub>2</sub> sample), a white precipitate was obtained as stated in the earlier section and then it was filtered and washed with hot water in the similar way. Then separately 0.4246 g of AgNO<sub>3</sub> (LR, Thomas Baker) was added to 100 mL of distilled water and 20% of NaOH (LR, Nice Chemicals) solution was added to it drop by drop. A brown precipitate was then observed and filtered it through G4 Gooch Crucible. Few portion of Ag might be washed out during washing by warm water. The white precipitate and the brown precipitate were taken together in a beaker and dissolved it in Acetic

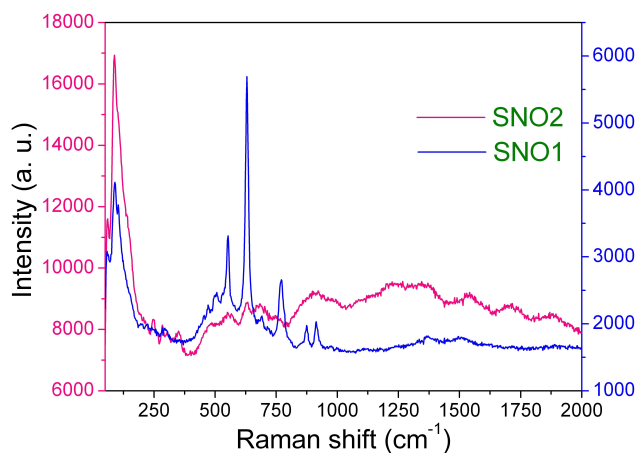


**Figure 2.** Raman spectra of the synthesized two doped SnO<sub>2</sub> samples.

acid. The mixture was added to the PVA solution (2 g of PVA in 50 mL of distilled water). The solution was stirred on a magnetic stirrer for 4 hours and then placed it in a hot air oven for 2 hours. After that, this was kept in a silica crucible at 800°C for another 2 hours.

### 3. Sample characterization

#### 3.1 X-ray powder diffraction

The X-ray powder diffraction patterns of the doped SnO<sub>2</sub> samples has been taken at ambient temperature in a X'Pert PRO Diffractometer (PW 3040/60, PANanalytical) operating at 45 kV and 40 mA, using Ni filtered CuK<sub>α</sub> radiation. The data were collected in step scan mode within the 2θ range 20° – 120° with a step size of 0.02° 2θ and the counting time of 10 sec per step for having good signal to noise ratio. To determine the instrumental profile, the diffraction pattern of fully recrystallized Si powder [33] was recorded with similar slits system.

#### 3.2 Scanning electron microscopy

Field emission scanning electron microscopy (FESEM) images of the samples were recorded in M/s Carl Zeiss, Sigma 300 and the elemental distribution/mapping is revealed from respective FESEM energy dispersive X-ray (EDX) spectrum.

#### 3.3 Raman spectroscopy

Raman measurements were performed in backscattering geometry using LABRAM HR (JobinYvon) spectrometer equipped with air-cooled argon (Ar<sup>+</sup>) ion laser of wavelength 488 nm and a Peltier cooled charge-coupled device (CCD) detector. The measurements were performed at room temperature.

#### 3.4 FTIR spectroscopy

The Fourier transformed infrared (FTIR) spectra of the samples were collected using a IRAffinity-1S, Shumadzu, FTIR spectrophotometer in the range 400–4000 cm<sup>-1</sup> for both of the samples.

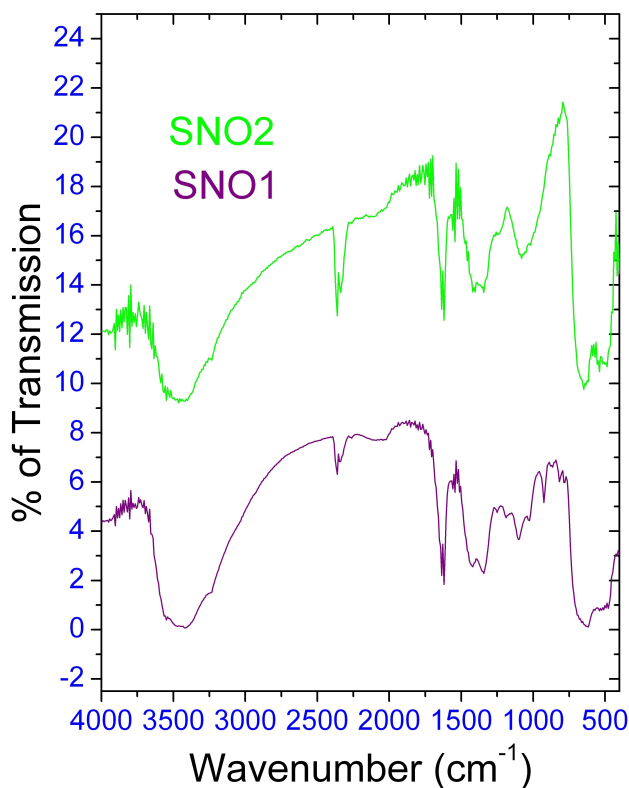


**Figure 3.** FTIR spectra of the synthesized two doped SnO<sub>2</sub> samples.

#### 3.5 Anti-microbial activity

Antibacterial activities of the isolated doped tin oxide samples were tested in vitro against two Gram-negative bacteria *Escherichia coli* (MCC2413), *Enterobacter aerogenes* (MCC3092) and one Gram-positive bacteria *Staphylococcus aureus* (MCC 2408) using agar disc diffusion method [34, 35] by NCCLS (National Committee for Clinical Laboratory Standards, 1997, India). The nutrient agar (Hi-Media Laboratories Limited, Mumbai, India), was autoclaved at 121°C at 1 atmosphere pressure for 15-20 minutes. The sterile-nutrient media was kept at 45-50°C. Then 100 μL of bacterial suspension containing 1.5 × 10<sup>8</sup> colony forming units (CFU)/mL were mixed with sterile liquid nutrient agar and poured into the sterile petri dishes. Upon solidification of the media, filter disc (5 mm diameter) was individually soaked with concentration of 500 μg/mL of each compound and placed on the nutrient agar media plates. The plates were incubated for 24h at 37°C. The diameter of the zone of inhibition (including disc diameter of 5 mm) was measured. Each experiment was performed in triplicate to minimize errors and the mean values were accepted.

## 4. Results and discussion

#### 4.1 X-ray powder diffraction analysis

Formation of rutile-type AB<sub>2</sub> structure for SnO<sub>2</sub> is evident from the X-ray diffraction patterns and is shown in figure 1.

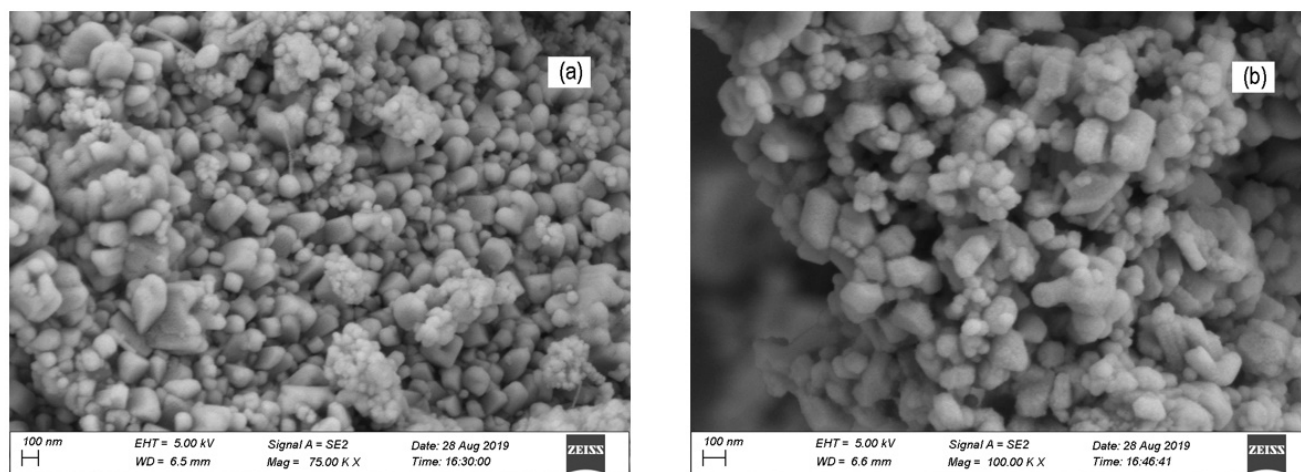


**Figure 4.** The FESEM images of the synthesized SnO<sub>2</sub> samples (a) SNO1 (b) SNO2.

For the Boron doped sample SNO1, no additional reflections have been observed, other than that of SnO<sub>2</sub> having tetragonal symmetry with space group P4<sub>2</sub>/mm, consistent with the JCPDS file number 41-1445. This indicates complete incorporation of Boron into the tetragonal lattice of SnO<sub>2</sub>. However, for the co-doped sample SNO2, an additional impurity phase for pure Silver has been identified as a secondary phase. This, in turn, indicates partial/ no substitution of Ag into the SnO<sub>2</sub> matrix. The diffraction peaks for the SNO1 sample appear to be broader than that of SNO2 samples, pointing out larger disorder due to reduced crystallinity. It can thus be argued that increasing Boron concentration either reduces the crystallite size or microstrain or both as evident from the progression of x-ray line broadening. Therefore, a quantitative phase analysis and a detailed structural analysis is required. In addition to structural analysis a difference in broadening of the two samples suggest different microstructural characteristics of the doped SnO<sub>2</sub> samples. Such a detail structural and microstructural analysis has been done using modified Rietveld Method.

The modified Rietveld analysis was performed by using the software MAUD [36] for simultaneous structural and microstructural refinement in addition to quantitative phase analysis, as required for the co-doped SnO<sub>2</sub> sample SNO2. In

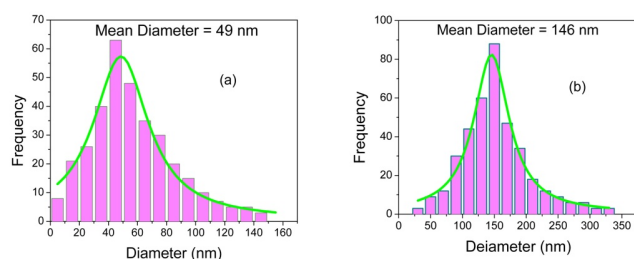


**Figure 5.** The histogram obtained from the FESEM images and the particle size distribution of the synthesized (a) SNO1 and (b) SNO2 samples.

MAUD the whole diffraction pattern is fitted simultaneously with pseudo-Voigt type profile shape function. The microstructure related parameters such as crystallite size or lattice microstrain are incorporated in the profile shape function and are the refinable parameters along with the structural parameters such as lattice parameter, thermal parameters, occupancy and atomic displacements, as described elsewhere [37]. Figure 1 shows the indexed fitted patterns along with the corresponding residuals. The accuracy of the refinement is judged by the reliability parameters [38], listed in Table 1. Here isotropic size-strain model has been considered as obtained from preliminary investigation of the nature of changes in profile broadening with the diffraction angles. Table 1 also summarizes

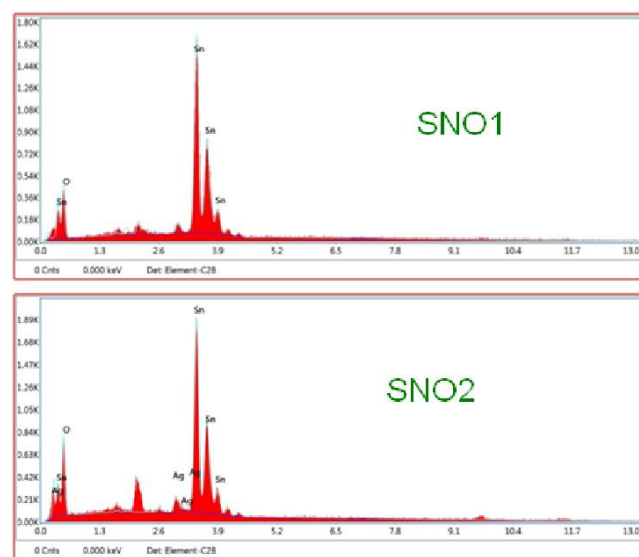


**Figure 6.** EDX spectrum of SNO1 and SNO2 samples. For SNO1, the wt% and atomic% of Sn:O are 86.88:13.11 and 50.26:49.73, whereas for SNO2, these ratios of Sn:Ag:O are 80.79:3.08:16.13 and 39.64:1.66:58.70 respectively.

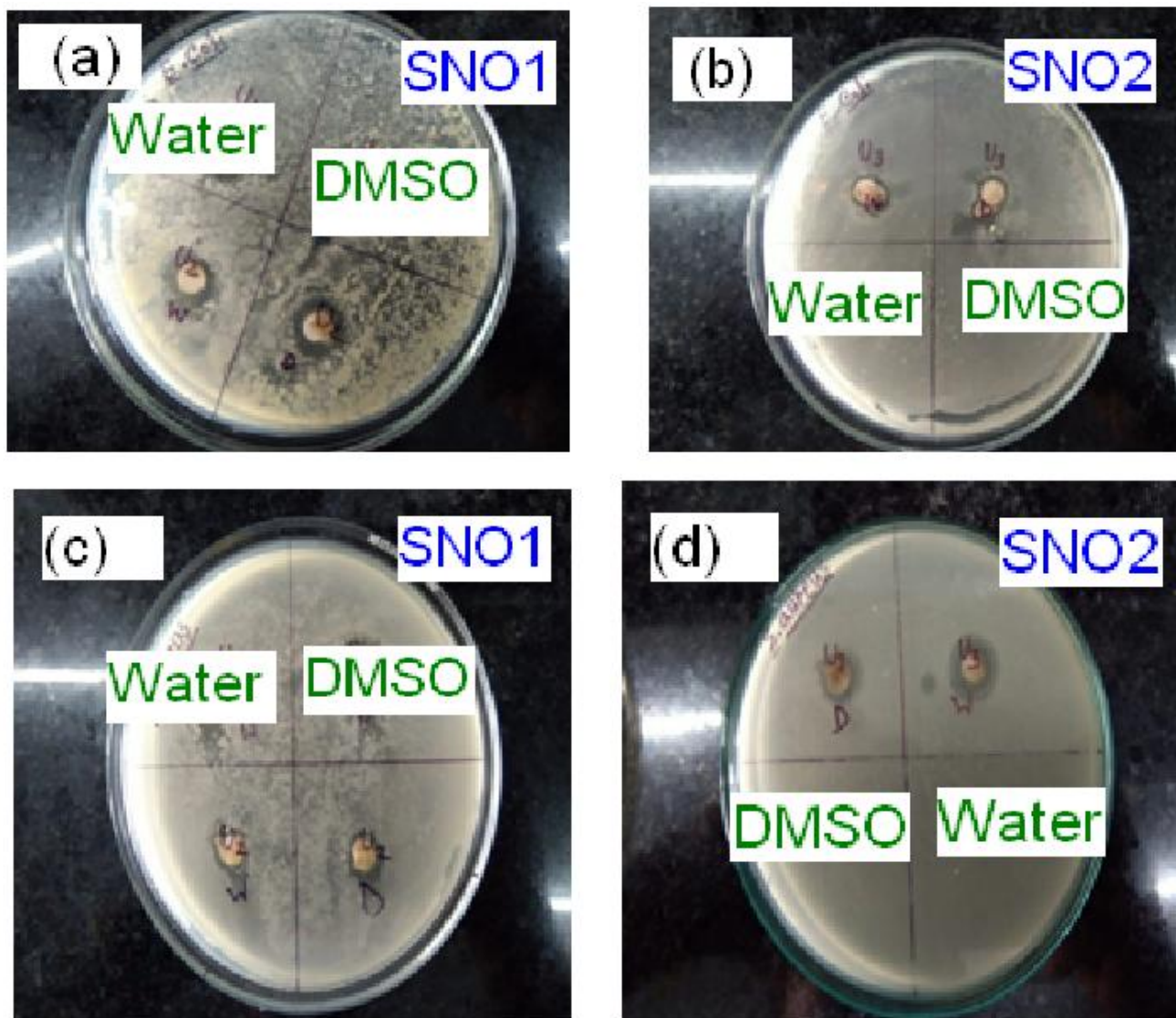


**Figure 7.** Response of synthesized SNO1 and SNO2 samples in water and DMSO media against *Escherichia coli* (a,b) and *Staphylococcus aureus* (c,d).

the refined value of weight fractions, positional co-ordinates, microstructural parameters etc. of the synthesized samples. The lattice parameters of pristine  $\text{SnO}_2$  samples are  $a = 4.7382\text{\AA}$  and  $c = 3.1871\text{\AA}$  respectively. For the synthesized doped tin oxide samples these cell parameters are given in Table 1. From the table, it is evident that the cell parameters for the doped samples are higher than that of the pristine samples and indicates that both B and Ag can be successfully doped into the host  $\text{SnO}_2$  lattice. However the lattice parameter of only B doped sample (SNO1) is slightly less than that of co-doped sample SNO2. This can be explained as, with the incorporation of boron having lesser ionic radius ( $0.23\text{\AA}$ ) than  $\text{Sn}^{+4}$  ( $0.71\text{\AA}$ ), significant distortion is produced in the  $\text{SnO}_2$  lattice. However, there is controversy whether B replaces the Sn atoms or it occupies interstitial position [21]. Recent reports of ab-initio DFT calculation on B-doped  $\text{SnO}_2$  [39] throws

some light on the possible dopant sites of Boron. It was observed that B doping in the interstitial position improves the photocatalytic property of B-doped  $\text{SnO}_2$ . DFT calculation indicated that when Boron occupies a substitutional site a decrease in lattice parameter is predicted, whereas an increase in lattice parameter is predicted for interstitial doping. Slightly higher lattice parameter observed in the present case, thus confirms the proposition of interstitial doping of Boron atoms in the host  $\text{SnO}_2$  lattice.

For rutile-type structure,  $\text{SnO}_2$  has two Sn-O bond distances, as evident from table 1. For apical Sn-O distance, O atoms are at  $\pm(x, x, 0)$ ; whereas for equatorial Sn-O distance, O atoms are at  $\pm(0.5-x, 0.5-x, \pm 0.5)$ . The average apical Sn-O bond length decreases to  $1.9947\text{\AA}$  for the SNO1 sample from the value of  $2.0172\text{\AA}$  for SNO2 sample due to decrease in oxygen position parameter. However, for the equatorial bond dis-

tance,  $c/a$  and  $O_x$  have opposite effects. The equatorial Sn-O bond length increases with the ratio  $c/a$ , where as it decreases with the increase in  $O_x$ . For the present case, an increase in equatorial Sn-O bond length has been observed from doped to co-doped sample. Further, as  $O_x$  being smaller for boron doped sample, the closest O-O distance along the shared edge ( $d_s$ ) of the  $\text{SnO}_6$  octahedra, increases in to reduce the electrostatic repulsion. It has been shown for group 14 rutile-type metal oxides that the ratio of the O-O distances along the shared edge to the unshared edge ( $d_u$ ) increases with the increase in cell volume due to reduction of O-O repulsions [40]. Similar trends have been observed for the as-prepared boron doped and silver-boron co-doped  $\text{SnO}_2$  samples.

The coherent domain/ crystallite size of the SNO1 sample is obtained to be 35 nm. The value of crystallite size is higher than that observed by Rajeswari et al. [17] for pure  $\text{SnO}_2$ . Similarly smaller values of crystallite sizes were obtained for co-doped  $\text{SnO}_2$  [16]. However the values obtained by the authors [16, 17] ignored the presence of microstrain in the samples. We have obtained small microstrains of the order of 0.2% in the co-doped samples. However the value of microstrain is lower for only Boron doped samples. Thus it appears that increasing the boron content does not result in an increase of microstrain but it increases with Ag addition. The value of crystallite size for co-doped sample is 98 nm which is higher compared to only boron doped sample, as predicted from the initial visual observation of the diffraction profile broadening.

#### 4.2 Raman and FTIR spectroscopy analysis

$\text{SnO}_2$  belongs to  $D_{4h}^{14} / P4_2 / mnm$  symmetry group. Group theory analysis provides that  $\text{SnO}_2$  has six vibrational modes. Among them,  $A_{1g}$ ,  $B_{1g}$ ,  $B_{2g}$  and  $E_g$  modes are Raman active while  $A_{2u}$  and  $E_u$  vibration modes are IR active. It has also been reported that  $B_{1g}$  mode of  $\text{SnO}_2$  is observed in the region of  $50 - 100 \text{ cm}^{-1}$ , when the particle size is less than 7 nm whereas  $E_g$ ,  $A_{1g}$  and  $B_{2g}$  modes appear in the high-frequency region  $450 - 775 \text{ cm}^{-1}$ , for large-sized particles. To probe all the vibrational modes we have performed both Raman and infrared spectroscopy. Figure 2 shows the Raman spectra of different concentration of boron (B) doped and silver-boron co-doped  $\text{SnO}_2$ . Raman spectra for all the samples show a peak at  $\sim 90 \text{ cm}^{-1}$  corresponds to  $B_{1g}$  vibration mode as

shown in Fig. 2. The presence of the peak in our samples having particle size much higher than 7 nm (see previous subsection) indicates that the incorporation of B into  $\text{SnO}_2$  lattice activate the mode.

At the higher frequency range, we have found peaks at  $551 \text{ cm}^{-1}$ ,  $630 \text{ cm}^{-1}$ ,  $690 \text{ cm}^{-1}$  and  $772 \text{ cm}^{-1}$ . Among them  $630 \text{ cm}^{-1}$  ( $A_{1g}$ ) mode is strongest and is related to the symmetric vibrations of Sn-O bonds [42]. The  $772 \text{ cm}^{-1}$  peak is assigned as  $B_{2g}$  which is attributed to asymmetric vibrations of Sn-O bonds [41]. The bands at  $551 \text{ cm}^{-1}$  and  $690 \text{ cm}^{-1}$  are due to vacant sites and local lattice disorder [42] and are assigned as S2 and S3 respectively [43]. The broadening of the Raman modes of all the samples with the increase of B concentration indicates crystal distortion [41] caused by incorporation of dopant into  $\text{SnO}_2$  lattice. It has been reported that the broadening of the strongest mode of  $\text{SnO}_2$  at  $630 \text{ cm}^{-1}$  ( $A_{1g}$ ) is related to the decrease of crystallite size [41] which can be determined from FWHM of the Raman spectra using the equation,  $\Gamma = 10 + 124.7/D$ ,  $\Gamma$  ( $\text{cm}^{-1}$ ) is the FWHM of  $A_{1g}$  mode and D is particle size in nm [44]. The calculated particle size is 19 nm for only Boron doped  $\text{SnO}_2$ . The difference between particle size obtained from Raman and XRPD analysis is due to the fact that both the techniques is not a direct method to estimate the size. In Ag-B co-doped sample the huge reduction of the intensity of  $A_{1g}$ ,  $B_{2g}$  and  $E_g$  mode might be the indication of a significant change of  $\text{SnO}_2$  crystal structure. XRPD analysis reveals a larger microstrain in co-doped samples.

Figure 3 shows the room temperature FTIR spectra of a B doped and Ag-B co-doped samples. There is no remarkable difference in the pattern of both the samples indicating absence of any chemical bonding in the doped state. The peaks appeared at approximately at  $540$  and  $625 \text{ cm}^{-1}$  are attributed to Sn-O and Sn-O-Sn vibrations respectively [41]. The two sharp absorption bands appeared at around  $1620 \text{ cm}^{-1}$  and  $1410 \text{ cm}^{-1}$  in both the samples originated from  $E_u$  and  $A_{2u}$  vibration modes of  $\text{SnO}_2$ , respectively. The band found in the range  $3140 - 3640 \text{ cm}^{-1}$  corresponds to stretching vibrational mode of surface hydroxyl group of water absorbed during the sample preparation [41, 45].

#### 4.3 FESEM and EDX study

The morphological and chemical analysis of the doped  $\text{SnO}_2$  samples have been carried out by field emission electron microscopy and energy dispersive x-ray spectroscopy attached to the FESEM. The FESEM images are shown in Fig. 4. The distributions of particle size for both SNO1 and SNO2 are obtained from the respective histograms as shown in Fig. 5. For either of the cases, the mean particle size and hence the average distribution is obtained on fitting by a lognormal function. The mean particle sizes thus obtained for SNO1 and SNO2 are 49 nm and 146 nm respectively. The particle size distribution of only Boron-doped  $\text{SnO}_2$  is however wider than that of  $\text{SnO}_2$  nanoparticles co-doped with Boron and Silver. From the Rietveld analysis of the whole profile x-ray powder

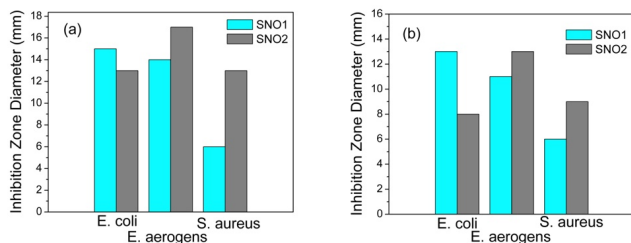


**Figure 8.** Histogram for the measured inhibition zone of SNO1 and SNO2 samples in both (a) water and (b) DMSO media in presence of various pathogenic bacteria.

diffraction pattern with isotropic microstructural model, it has been observed in the section 3.1 that, the corresponding average crystallite sizes obtained are 35 nm and 98 nm. Since, an area averaged values of crystallite size is obtained from x-ray powder diffraction, the findings from FESEM study for both the as-prepared samples SNO1 and SNO2 are in gross agreement with the corresponding results obtained from x-ray powder diffraction profile analysis.

Figure 6 shows the EDX spectrum of the two samples. An accelerating voltage of 20 kV has been applied to record the EDX spectrum for both SNO1 and SNO2. The spectrum confirms the presence of tin (Sn) and oxygen (O) for SNO1 and Sn, O and silver (Ag) for SNO2 sample along with some trace amount of impurity elements in both the cases. It is observed from the EDX spectrum that the existence of boron could not be estimated qualitatively and hence quantitatively in either of the cases. It can be explained as boron being the lighter element ( $Z \leq 9$ ) has only the K peak present and it is in the energy range below 1 keV, thus often causing interference with the other family of peaks of the heavier elements, appeared in that energy span. This makes its identification difficult due to large peak overlap. Also because of low yield of x-rays and large self-absorption by the lighter elements like boron, the peak intensity often becomes very close to the electrical noise of the detecting system. However, if the accelerating voltage could have been optimized to a suitable lower value, existence of boron might be established.

**Table 1.** Structural and microstructural parameters obtained from the Rietveld analysis of X-ray powder diffraction pattern for the synthesized doped SnO<sub>2</sub> samples.

Sample	SNO1	SNO2
Relative Wt%	1.0	0.92 (1)
a:	4.7394 (3)	34.7403 (4)
Cell (Å) c:	3.1869 (5)	3.1879 (2)
Size (nm)	35 (1)	98 (2)
Strain ( $\times 10^4$ )	0.5 (4)	2.7 (1)
O <sub>x</sub>	0.2976 (6)	0.3009 (5)
B <sub>isoSn</sub>	0.244 (13)	0.188 (12)
B <sub>iso</sub> O	0.190 (40)	0.188 (equal)
Cell vol. (Å <sup>3</sup> )	71.58	71.63
(c/a) ratio	0.672	0.673
Sn-O (Å)(apical)	1.995	2.017
Sn-O (Å)(equatorial)	2.093	2.079
d <sub>s</sub> (Å)	2.713	2.669
d <sub>u</sub> (Å)	3.187	3.188
R <sub>wp</sub>	5.548	5.696
R <sub>b</sub>	4.425	4.571
Gof	1.150	1.161

#### 4.4 Anti-microbial activity study

Agar disc diffusion method was used for the study of antibacterial activity of the synthesized doped tin-oxide nanoparticles against some Gram-positive and Gram-negative bacteria which are close to corresponding human bacteria pathogens, causing various infections. Antibacterial activity of the two doped SnO<sub>2</sub> samples against the chosen bacteria in water and DMSO media were evaluated on the basis of inhibition zone (mm) as shown in Fig. 7. From Fig. 8 it is evident that sample SNO2 nanoparticles have a significant antibacterial activity against *Staphylococcus aureus* (MCC2408) and *Enterobacter aerogenes* (MCC3092) in both water and DMSO. However, sample SNO1 is more effective against *Escherichia coli* (MCC2413) in water and as well as DMSO media also. These observed different antibacterial response for the as prepared boron doped and boron-silver co-doped tin oxide nanoparticles may be due to the cumulative effects of smaller crystallite size, different surface morphologies and other factors like for the presence of different reactive oxygen species and oxygen vacancies in the material.

## 5. Conclusion

Boron doped nanocrystalline SnO<sub>2</sub> and boron and silver co-doped SnO<sub>2</sub> was prepared by a simple sol-gel method. X-ray powder diffraction was used for the structural and microstructural characterization of nanocrystalline materials. A modified Rietveld method was used to determine both the structural parameters and microstructural parameters simultaneously. Raman spectroscopy, Fourier transformed infrared Spectroscopy and Scanning Electron Microscopy was used for chemical and morphological characterization. The FTIR-Spectra reveals the incorporation of B and Ag in the SnO<sub>2</sub> matrix. The XRPD pattern of the as prepared sample demonstrated the formation of a rutile structure of SnO<sub>2</sub> nanocrystallites of average particle size of 35 nm and 98 nm of SNO1 and SNO2 samples respectively. A significant lattice microstrain was observed for the Ag-B co-doped SnO<sub>2</sub> samples in accordance with the FTIR studies. Significant anti-microbial activities against some Gram-Positive & Gram-Negative bacteria were observed for both the samples in water and DMSO medium due to the cumulative effects of smaller crystallite sizes and surface morphologies.

#### Conflict of interest statement:

The authors declare that they have no conflict of interest.

## References

- [1] A.S. Fauci, N.A. Touchette, and G.K. Folkers. *Emerg. Infect. Dis.*, **11**:519, 2005.
- [2] S.M. Dizaj, F. Lotfipour, M. Barzegar-Jalali, M.H. Zarrintan, and K. Adibkia. *Mat. Sc. Eng. C.*, **44**:278, 2014.
- [3] R. Birringer. *Mater. Sci. Eng. A.*, **117**:33, 1989.
- [4] J.B. Wright, K. Lam, D. Hansen, and R.E. Burrell. *Am. J. Infect. Control*, **27**:344, 1999.

- [5] A.M. Allahverdiyev, E.S. Abamor, M. Bagirova, and M. Rafailovich. *Future Microbio.*, **6**:933, 2011.
- [6] A. Besinis, T. De Peralta, and R.D. Handy. *Nanotoxicol.*, **8**:745, 2014.
- [7] M. Ghosh, M. Mondal, S. Mandal, A. Roy, S. Chakrabarty, G. Chakrabarti, and S.K. Pradhan. *J. Mol. Struct.*, **1211**:128076, 2020.
- [8] X.D. Zhao, S.P. Deng, W.F. Pan, N. Qi, Z.Q. Chen, X.L. Su, and X.F. Tang. *J. Mat. Sci.*, **56**:2360, 2021.
- [9] K. Thiyagarajan and K. Sivakumar. *J. Mat. Sci.*, **52**:084, 2017.
- [10] Y. Feng, B.J. Huang, S.S. Li, B.M. Zhang, W.X. Ji, C.W. Zhang, and P.J. Wang. *J. Mat. Sci.*, **50**:6993, 2015.
- [11] L.C. Nehru, V. Swaminathan, and C. Sanjeeviraja. *Am. J. Mat. Sci.*, **2**:6, 2012.
- [12] P. Mukherjee, S. Senapati, D. Mandal A. Ahmad, M.I. Khan, R. Kumar, and M. Sastry. *Chem Bio Chem.*, **3**:461, 2002.
- [13] K.C. Bhainsa and S.F. Dsouza. *Colloids Surf. B: Bioint.*, **47**:160, 2006.
- [14] H.S. Nalwa. *nanostructured materials and nanotechnology*. Academic Press, 1th edition, 2000.
- [15] N. John, M. Somaraj, and N.J. Tharayil. *IOP Conf. Series: Mater. Sci. Eng.*, **360**:012007, 2018.
- [16] A. Fakhri, S. Behrouz, and M.Pourmand. *J. Photochem. Photobiol. B: Biol.*, **149**:45, 2015.
- [17] S. Rajeswari, J.U. Maheswari, D. Muthuraj, E. Kumar, and V. Veeraputhiran. *J. Nanosci. Tech.*, **5**:637, 2019.
- [18] A.H.T. Nguyen, M.C. Nguyen, H. Ji, J. Cheon, K. Yu, J. Kim S. Kim, S. Cho, R. Choi, H.P Pham, and Q.T. Tran. *J. Vacu. Sci. Tech. B*, **36**:062203, 2018.
- [19] P.S. Kolhe, P.M. Koinkar, N. Maiti, and K.M. Sonawane. *Physica B: Cond. Mat.*, **524**:90, 2017.
- [20] K.K. Nair, P. Kumar, V. Kumar, R.A. Harris, R.E. Kroon, B. Viljoen, P.M. Shumbula, M. Mlambo, and H.C. Swart. *Physica B: Cond. Mat.*, **535**:338, 2018.
- [21] B. Zhang, Y. Tian, J.X. Zhang, and W. Cai. *Vacuu.*, **85**:986, 2011.
- [22] X.B. Kong, F. Li, Z.N Qi, L. Qi, and M.M. Yao. *Surf. Rev. Lett.*, **24**:1750059, 2017.
- [23] Z. Nasir, M. Shakir, R. Wahab, M. Shoeb, P. Alam, R.H. Khan, and M. Mobin. *Int. J. Bio. Macromol.*, **94**:554, 2017.
- [24] A.K. Singh and U.T. Nakate. *Adv. Nano.*, **2**:66, 2013.
- [25] A.A. Firooz, A.R. Mahjoub, and A.A. Khodadadi. *Mat. Lett.*, **62**:1789, 2008.
- [26] E.R. Leite, I.T. Weber, E. Longo, and J.A. Varela. *Adv. Mat.*, **12**:965, 2000.
- [27] C. Nayral, E. Viala, P. Fau, F. Senocq, J.C. Jumas, A. Maisonnat, and B. Chaudret. *Chem. Euro. J.*, **6**:4082, 2000.
- [28] J. Zhu, Z. Lu, S.T. Aruna, D. Aurbach, and A. Gedanken. *Chem. Mat.*, **12**:2557, 2000.
- [29] G. Pang, S. Chen, Y. Koltypin, A. Zaban, S. Feng, and A. Gedanken. *Nano Lett.*, **1**:723, 2001.
- [30] V. Subramanian, W.W. Burke, H. Zhu, and B. Wei. *J. Phys. Chem. C.*, **112**:4550, 2008.
- [31] J. Jouhannaud, J. Rossignol, and D. Stuerger. *J. Solid State Chem.*, **181**:439, 2008.
- [32] C.L. Ma and X.D. Sun. *Nanotech.*, **13**:565, 2002.
- [33] J.G.M. van Berkum, G.J.M. Sprong, Th.H. de Keijser, R. Delhez, and E.J. Sonneveld. *Powder Diffr.*, **10**:129, 1995.
- [34] A.W. Matthew, R.C. Franklin, A.C. William, N.D. Michael, and M.E. George. *Performance standards for antimicrobial disc susceptibility test*. Clinical and Laboratory Standards Institute, 9th edition, 2006.
- [35] W. Pa. *Methods for dilution antimicrobial susceptibility tests for bacteria that grow aerobically*. Clinical and Laboratory Standard Institute, 3th edition, 2006.
- [36] L. Lutterotti, S. Matthies, and H.R. Wenk. *IUCr. Newsl. CPD.*, **21**:14, 1999.
- [37] A.K. Deb, P. Chatterjee, and S.P. SenGupta. *Actamater.*, **52**:2755, 2004.
- [38] A.K. Deb, P. Chatterjee, and S.P. SenGupta. *Mat. Sci. Eng.: A.*, **459**:124, 2007.
- [39] P.P. Filippatos, N. Kelaidis, M. Vasilopoulou, D. Davazoglou, and A. Chronos. *Scientific Reports.*, **11**:1, 2021.
- [40] A.A. Bolzan, C. Fong, B.J. Kennedy, and C.J. Howard. *Acta Cryst. Sec. B: Struc. Sci.*, **53**:373, 1997.
- [41] A. Ahmed, M.N. Siddique, T. Ali, and P. Tripathi. *Appl. Surf. Sci.*, **483**:463, 2019.
- [42] P. Sangeetha, V. Sasirekha, and V. Ramakrishnan. *J. Raman Spec.*, **42**:1634, 2011.
- [43] A. Dieguez, A. Romano-Rodriguez, A. Vila, and J.R. Morante. *J. Appl. Phys.*, **90**:1550, 2001.
- [44] S. Soni, S. Kumar, B. Dalela, S. Kumar, P.A. Alvi, and S. Dalela. *J. Alloys Comp.*, **752**:520, 2018.
- [45] M. Aziz, S.S. Abbas, and W.R.W. Baharom. *Mat. Lett.*, **91**:31, 2013.